Proceedings of
ASME Turbo Expo 2012, June 11-15, 2012, Copenhagen, Denmark

GT2012-68150

SIMULATION OF NON-SYNCHRONOUS BLADE VIBRATION OF AN AXIAL COMPRESSOR USING A FULLY COUPLED FLUID/STRCUTURE INTERACTION

Hong-Sik Im *
Ge-Cheng Zha†
Dept. of Mechanical and Aerospace Engineering
University of Miami
Coral Gables, Florida 33124
E-mail: gzha@miami.edu

ABSTRACT

In this paper non-synchronous vibration (NSV) of a GE axial compressor is simulated using a fully coupled fluid/strcuture interaction (FSI). Time accurate Navier-Stokes equations are solved with a system of 5 decoupled structure modal equations in a fully coupled manner. A 3rd order WENO scheme for the inviscid flux and a 2nd order central differencing for the viscous terms are used to resolve nonlinear interaction between vibrating blades and fluid flow. $1/7$*th annulus is used with a time shifted phase-lag (TSPL) boundary condition to reduce computational efforts. A fully conservative rotor/stator sliding boundary condition is employed to accurately capture unsteady wake propagation between the rotor and stator blades. The predicted dominant frequencies using the blade tip response signals are not harmonic to the engine order, which is the NSV. The blade vibration is torsionally coupled with highly oscillating blade pressure and is not damped out during the NSV. No resonance to the blade natural frequencies is found. The instability of tornado vortices in the vicinity of the rotor tip due to the strong interaction of incoming flow, tip vortex and tip leakage flow is the main cause of the NSV observed in this study.*

1 Introduction

Turbomachinery aeromechanic problems are very challenging since they involve both aerodynamics and structural vibration. Blade vibration due to forced response and flutter have been studied for decades with the progress of improving turbomachinery efficiency and reliability. Recently, a new turbomachinery aeromechanic problem, namely non-synchronous vibration(NSV), whose blade vibration frequency is away from harmonics of rotor shaft frequency, has attracted a lot of attention [1–8]. The present study shows that NSV has no resonance with the rotor blades, while flutter is a self-excited aeroelastic instability at or close to the rotor blade natural frequency [1, 9].

Rotating instability (RI) is considered as one cause of NSV [1–4]. The experiment for the 10 stage high pressure axial compressor by Baumgartner et al. [1] shows that for a certain operating condition high vibration levels on the first stage blades exist. The frequencies are not in resonance with engine orders. A rotating flow instability revolves relative to the blade row similar to rotating stall cell. The velocity fluctuations measured by the Hot-film probe near the blade trailing edge show the radial dependency of this rotating instability. The frequencies of the rotating instability are visible at 91% blade span with high coherence level, , which is decaying away from the RI center, and eventually at 65% blade span the RI is no more detectable.

Kielb et al. [2] conducted an experimental and numerical investigation for a full size compressor rig where blade-mounted strain gages and case-mounted unsteady pressure transducers are devised to measure the NSV. The experimental strain gage data show step change in frequency as the compressor operating condition varies. This is another feature of the NSV. The stage 1 rotor blades experience a significant NSV response of 2661 Hz at 12700 rpm near first torsional mode (or 2nd mode natural frequency) and exhibit the

*Ph.D. Student, ASME Member
†Associate Professor, ASME Senior Member

NSV frequency shift from 2661 to 2600 Hz at 12800 rpm. At the casing, the NSV frequencies of 3516 Hz and 3662 Hz are measured in the non-rotating reference frame. Their numerical results for the 1/7th rotor annulus rotor indicate a suction side vortex shedding and a tip flow instability near 75% span as the excitation source of the NSV.

The work of Marz et al. [3] also shows the rotating instability as a main source for NSV. A low speed single stage fan with outlet guide vanes is used for their experimental and numerical study on the NSV. The rotor design speed is 3000 rpm and has the blade passing frequency (BPF) of 560Hz. They tested four different tip clearances of 0.7%, 1.4%, 2.8%, and 5.6% tip axial chord at near the maximum fan loading condition. The measured wall pressure spectrum shows a NSV frequency at roughly half of BPF. The time-lapse plots of casing wall pressure indicate that the flow intensity varies from blade to blade with the presence of a high fluctuating flow instability in the rotor entry plane for tip clearances of 2.8% and 5.6%. It turns out that the blade sensor signal near the rotating instability has a strong periodic content. A vortex structure moving from the suction side to the pressure side is observed in the middle of the blade passage by the full annulus simulation for 2.8% tip clearance, which is the main causes of unsteadiness when the rotating instability develops. The numerical study shows no tip spillage flow even with the rotating instability.

Mailach et al. [4] carried out an experimental study of a low speed research compressor to investigate influence of tip clearance and operating point on rotating instability. Rotating instability have been found at a tip clearance of 3% tip axial chord. At a larger tip clearance of 4.3%, the rotating instability is fully developed for all the rotor speeds including 50%, 80%, and 100% design speed. The formation of rotating instability is limited to a narrow operating range near the stall boundary. The measurement at the casing wall shows a narrow band increase of the amplitudes in the frequency spectrum at about 30% of BPF. When the compressor approaches the stall boundary, the rotating instability shifts to slightly lower frequencies while amplitude of the perturbation grows. Measurements on the rotor blades show that the rotating instability is limited to the blade tip region. Maximum amplitudes appear at 92% of the blade height and 20% to 30% of chord length. For a large tip clearance a strong blade tip vortex is observed in the rotor tip region. The fluctuating blade tip vortices propagate in rotor circumferential direction. Tip clearance size is shown as the main influence parameter on the rotating instability.

Thomassin, et al. [5,6] suggested a theory different from the rotating instability to explain the NSV based on the resonance of a impinging jet vortex structure and the acoustic feedback of a vibrating plate. The jet core feedback theory has been proved by an experiment conducted in [5, 6]. It shows that when the acoustic reflection wave length equals to the jet-to-plate distance, the jet vortical structures lock-on to the acoustic wave frequency and significant amplification of the pressure fluctuation and vibration of the flexible plate are observed. They suggest a simple model to predict the critical tip velocity based on their impinging jet experiment. Vo [8]'s simulation shows a tip clearance flow instability for an isolated subsonic axial compressor rotor. In the blade tip region the trailing edge backflow causes flow impingement on the pressure side that leads to the flow unsteadiness associated with the NSV.

Im and Zha [10] investigate a 1-1/2 stage compressor NSV with different tip clearance size and shape. They observed that a tornado like tip vortex with vortex axis pointing to the suction surface near leading edge is the primary instability causing the NSV. Their simulation also indicates that the tip clearance shape has strong influence on the NSV intensity and frequency.

So far, all the aforementioned NSV studies use rigid blades with no blade vibration. The reason is that simulation of fluid-structural interaction is not straightforward. The goal of NSV simulation is to let engineers avoid NSV or decide if the vibration amplitudes are within the limits of structural strength and fatigue. A simulation with realistic fluid structural interaction (FSI) would be valuable to guide the rotor blade design. Such simulation will not only shed more light to reveal the flow physics of NSV, but also provide the blade structural response, which is crucial for blade aeromechanics design. This paper is to make the first effort to simulate compressor blade NSV with fluid structural interaction.

To accurately resolve nonlinearities of FSI, the governing equations of structural and fluid motion need to be simultaneously integrated in time. However, due to high CPU cost, many of the fluid-structural interaction simulations are implemented by a loosely coupled procedure, i.e., the structural response lags behind the flow solution by one or a few time steps. The information is exchanged after partial or complete convergence of individual solvers [11]. For example, Gnesin et al. [12] solved the unsteady Euler equations with the modal approach for the structure analysis in the partially coupled manner. Doi et al. [13] weakly coupled an explicit Runge-Kutta multigrid flow solver with a FEM structure solver to predict aeroelastic responses of NASA Rotor 67 blade. Carstens eta al. [14] and Sayma et al. [15] loosely integrate the equations of motion using Newmark scheme at each time step.

For the fully coupled fluid-structure interaction used in this study [16, 17], time accurate 3D compressible Navier-Stokes equations are solved with a system of 5 decoupled modal equations in a fully coupled manner. The flow field and structure always respond simultaneously by exchanging the unsteady aerodynamic force and structural displacement within each physical time step via a successive iteration on the pseudo-time step. An advanced moving mesh generation technique [17] that can significantly reduce mesh skewness at the rotor tip clearance is used. In addition, an efficient time-shifted BC is implemented and applied at lower/upper circumferential periodic boundaries to facilitate 1/7th annulus simulations.

The purposes of this paper are to capture the dominant blade frequencies of a GE high-speed axial compressor and to study a relevant flow mechanism that causes the NSV using the fully coupled fluid structure interaction. A rotor tip with clearance size of 2.4% tip chord is recommended by GE

Aviation for investigation.

Nomenclature

I	identity matrix
L_∞	blade chord at hub
p	static pressure
N_D	nodal diameter
T	period for one nodal diameter
U_∞	absolute velocity at inlet
Δt	physical time step
$\frac{\Delta S}{R}$	change of entropy, $\frac{\gamma}{\gamma-1} ln \frac{To}{To_\infty} - ln \frac{Po}{Po_\infty}$
Ω	rotor angular speed in *radians/sec*
ρ	air density
ϕ	sector of annulus circumferential angle
- Flutter parameters -	
b_s	bade root semi-chord
$\bar{m}$	blade mass
$\bar{V}$	frustum volume
V^*	reduced velocity, $\frac{U_\infty}{b_s \omega_\alpha}$
V_f	flutter speed index, $\frac{V^*}{\bar{\mu}}$
ω	blade natural frequency
ω_α	1st torsional mode natural frequency
$\bar{\mu}$	mass ratio, $\frac{\bar{m}}{\bar{V}\rho_\infty}$
- Abbreviations -	
NSV	non-synchronous vibration
$TSPL$	time shifted phase lag
$WENO$	Weighted Essentially Non-oscillatory

2 The NSV Compressor

A GE axial compressor (GE-C1 case) exhibits a NSV at the first stage rotor blades [2]. The first 1-1/2 stage with 56 IGVs, 35 rotor blades and 70 stator blades of the full compressor is used for current simulations. The rotor tip clearance of the compressor rig is 1.1% of tip chord. The measured blade NSV is a phase-locked response and close to 1st torsional blade natural frequency. The strain gage on the blade surface shows the NSV frequency of 2600 Hz at around 12880 RPM and 2661 Hz as the rotor speed slightly decreases to 12700 RPM as shown in Fig. 1.

3 Aerodynamic Model

The unsteady Reynolds-averaged Navier-Stokes (URANS) equations are solved in a rotating frame [18] with the Spalart-Allmaras (SA) turbulence model [19]. An accurate high order scheme in space is necessary for multistage axial compressors in order to rigorously resolve interaction effects such as wake and shocks between rotor and stator. In this study the Low Diffusion E-CUSP (LDE) Scheme [20] as an accurate shock capturing Riemann solver is used with a 3rd order WENO reconstruction for inviscid flux and a 2nd order central differencing for viscous terms [21]. An implicit 2nd order dual time stepping method [22] is solved using an unfactored Gauss-Seidel line iteration to achieve high convergence rate. The high-scalability parallel computing is

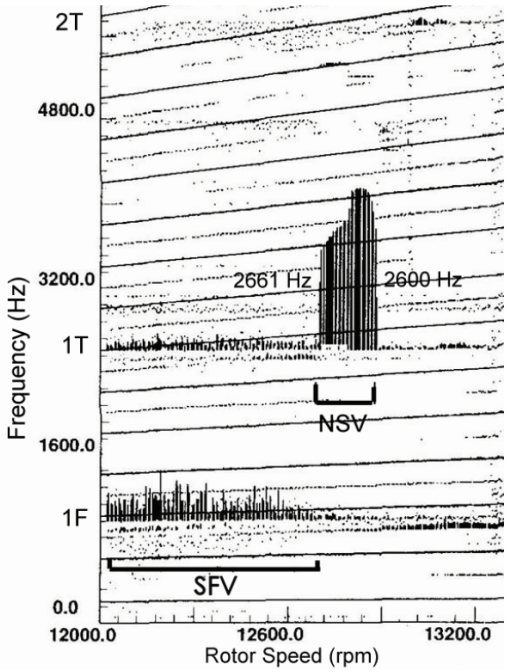

FIGURE 1: Strain gage response of the first-stage rotor blades of the high-speed compressor showing SFV(separated flow vibration) and NSV(non-synchronous vibration)

implemented to save wall clock time [23]. The interaction between rotating and stationary blades introduces inherent unsteadiness to the flow of multistage turbomachinery. For instance, the shock wave interaction between inter blade rows as well as rotating instabilities as a main driver of NSV can be predicted not by the steady approach, but only by the conservative unsteady approach. A fully conservative sliding BC [24] is used to solve the moving rotor in the rotating frame and the stator blades in the fixed frame.

3.1 Phase Lag Boundary Condition

To avoid calculation of full annulus rotor, a boundary condition needs to be setup on the circumferential boundaries of a sector of the rotor. The time shifted phase lag (TSPL) BC, also called direct store phase lag BC, suggested by Erods et al. [25] and Srivastava et al. [26] based on phase periodicity with the period as nodal diameter is utilized. The TSPL BC is selected for this study for its advantage that it does not need to input the primary perturbation or vibration frequencies required by the Fourier phase lag BC [27]. Such frequencies are not known *a priori*. In other words, the TSPL BC is more general than the Fourier phase lag BC, but still limited to the circumferential periodicity assumption, which does not exist when a rotating stall occurs.

As sketched in Fig. 2, let us assume that the rotor rotates from the upper circumferential boundary to the lower circumferential boundary such that information at the upper side is delayed by time δt. T is the period of one nodal diameter (N_D). To update the upper/lower circumferential

boundaries, first the conservative variables of the upper inner cells(Q_{IU}) and the lower inner cells(Q_{IL}) are stored for δt and $T-\delta t$ respectively. Then, these stored values are rotated by the circumferential angle of the sector geometry (ϕ) to update the boundary ghost cells of the other side. The upper ghost cell Q_{GU} at time t can be updated using Q_{IL} at time $T-\delta t$. However, the lower ghost cell Q_{GL} at time t can not be updated using the upper ghost cell values since Q_{IU} at time $t+\delta t$ is not available. The way to update Q_{GL} is to take one cycle-lagged value, Q_{IU} at time $T-t+\delta t$, by assuming phase periodicity as depicted in Fig. 2. Note that the boundaries are treated as in-phase condition for the first cycle since the stored Q at both sides are not available. In the current study N_D of 5 observed in the experiment is used to determine ϕ and T for 1/7th sector of the annulus.

$$Q_{GL}(t) = Q_{IU}(t+\delta t) = Q_{IU}(t-T+\delta t) \tag{1}$$

$$Q_{GU}(t) = Q_{IL}(t-\delta t) \tag{2}$$

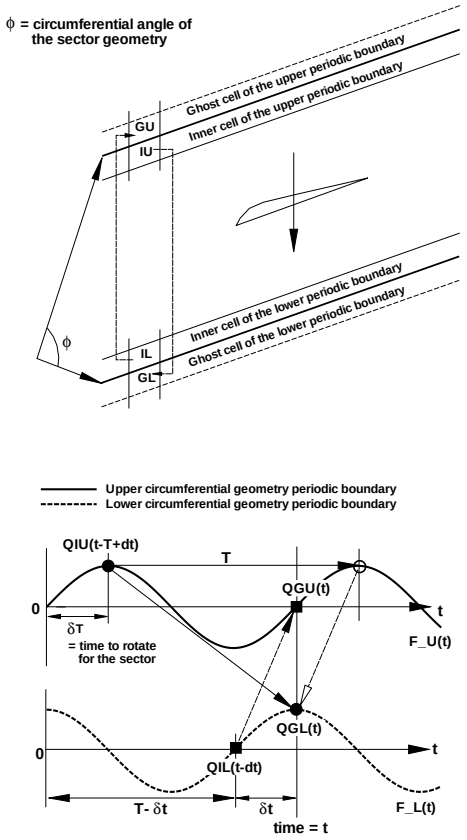

FIGURE 2: Sketch of the time shift phase lag BC showing how to define upper periodic ghost cell, Q_{GU}

3.2 Other Boundary Conditions

At the IGV inlet, the given radial distributions of total pressure, total temperature, swirl angle and pitch angle are applied and velocity is extrapolated from the computational domain in order to determine the rest of variables. On the blade surface and casing wall a non-slip boundary condition is applied, while on the hub surface the law of the wall is used to avoid an excessive fine mesh in the boundary layer [18]. At the stator outlet, the static pressure is specified in the spanwise direction. The velocity components are extrapolated from the computational domain and an isentropic relation is used to determine the density. If the wall surface is rotating, the wall static pressure for the inviscid momentum equation is determined by solving the radial equilibrium equation.

$$\frac{1}{\rho}\frac{\partial p_b}{\partial r} = \frac{V_\theta^2}{r} \tag{3}$$

If the wall surface is stationary, then the static pressure gradient across the wall boundary is set to zero. In addition, the adiabatic condition is used to impose zero heat flux through the wall.

4 Structural Model

For the rotating blades in the relative frame of reference, one can assume that the stiffness of the rotor disk is much larger than that of the compressor blades, the vibration characteristics of the blades is dominant such that rotor disk vibration effect is negligible.

4.1 Modal Approach

The equation of motion of an N-DOF(degree of freedom) system with the mechanical damping and the aerodynamic loading as the excitation force can be presented in matrix form:

$$[\mathbf{M}]\{\ddot{\mathbf{X}}\} + [\mathbf{C}]\{\dot{\mathbf{X}}\} + [\mathbf{K}]\{\mathbf{X}\} = \{\mathbf{F}\} \tag{4}$$

where, **M**, **C**, **K** are the mass, structural damping and stiffness matrices. **F** is the total aerodynamic force acting on the blade surface. The total aerodynamic force can be defined as follows:

$$\mathbf{F} = -\oint P\cdot\hat{n}dA + \oint \tau_{\mathbf{w}}\cdot\hat{t}dA \tag{5}$$

where, $\hat{n}$ is the unit normal vector to the blade surface and $\hat{t}$ is the unit tangent vector to the blade surface. P is the fluid static pressure and $\tau_{\mathbf{w}}$ is the fluid wall shear stress acting on the blade surface. It is demonstrated by Gruber and Carstens [28] that viscous effects can cause a significant difference in aerodynamic damping.

To decouple the equations of motion for the damped systems(4), we use the mass normalized mode shape($\tilde{\phi}$) de-

fined as the normal modes divided by square root of the the generalized mass($\sqrt{\phi^T m \phi}$). Let

$$\{\mathbf{X}\} = [\tilde{\Phi}]\{\mathbf{q}\} \tag{6}$$

and premultiply Eq. (4) by the transpose $[\tilde{\Phi}]^T$.

$$\begin{aligned}[\tilde{\Phi}]^T[\mathbf{M}][\tilde{\Phi}]\{\ddot{\mathbf{q}}\} + [\tilde{\Phi}]^T[\mathbf{C}][\tilde{\Phi}]\{\dot{\mathbf{q}}\} + [\tilde{\Phi}]^T[\mathbf{K}][\tilde{\Phi}]\{\mathbf{q}\} \\ = [\tilde{\Phi}]^T\{\mathbf{F}\}\end{aligned} \tag{7}$$

where $\mathbf{q}$ is the vector of the principal coordinates. Using the orthogonality of the system matrices and assuming damping matrix to be a linear combination of the mass and stiffness matrices, Eq. (7) is then completely decoupled and the jth equation will have the form

$$\ddot{q}_j + 2\zeta_j\omega_j\dot{q}_j + \omega_j^2 q_j = \frac{\tilde{\phi}_j^T}{m_j}\mathbf{F} \tag{8}$$

where $[\tilde{\Phi}]^T = [\tilde{\phi}_1, \cdots, \tilde{\phi}, \cdots, \tilde{\phi}_N]^T$. N is the number of modal coordinates. ω_j and ζ_j are natural frequency and modal damping ratio for mode j. Since structural damping of the blade is usually very small [29], ζ of 0.005 is used for all modes. m_j denotes the jth diagonal element of modal mass matrix which will be unity. In the current study, the structural system may be reduced to only five mode shapes, since a few bending and torsional frequencies are usually sufficient to determine flutter. The normalized modal equation can be given as [16]

$$\ddot{q}_j + 2\zeta_j(\frac{\omega_j}{\omega_\alpha})\dot{q}_j + (\frac{\omega_j}{\omega_\alpha})^2 q_j = \frac{\tilde{\phi}_j^{*T}}{m_j^*}\cdot\mathbf{F}^*\cdot {V_f}^2\cdot\frac{b_s^2 L_\infty}{\bar{V}}\cdot\bar{m} \tag{9}$$

where the dimensionless quantities are denoted by an asterisk. $V_f(=\frac{U_\infty}{b_s\omega_\alpha\sqrt{\bar{\mu}}})$ is the flutter speed index which is an input flutter control parameter. $\bar{m}$ is the measured blade mass, $\bar{V}$ represents the conical frustum volume and b_s is the streamwise root semi chord. L_∞ is the reference length and ω_α is the angular frequency of the first torsional mode in units $radians/sec$. $\bar{\mu}(=\frac{\bar{m}}{\bar{V}\rho_\infty})$ stands for the mass ratio, i.e. the ratio between the structural mass and the mass of the equivalent volume of fluid at reference density. It is noticed that m_j^* should be equal to one when the mass normalized mode shapes are used.

The equations are then transformed to a state form as follows:

$$[\mathbf{M}]\frac{\partial\mathbf{S}}{\partial t} + [\mathbf{K}]\{\mathbf{S}\} = \mathbf{q} \tag{10}$$

where

$$\mathbf{S} = \begin{pmatrix} q_j \\ \dot{q}_j \end{pmatrix}, \mathbf{M} = [I], \mathbf{K} = \begin{pmatrix} 0 & -1 \\ (\frac{\omega_j}{\omega_\alpha})^2 & 2\zeta_j(\frac{\omega_j}{\omega_\alpha}) \end{pmatrix}$$

$$\mathbf{q} = \begin{pmatrix} 0 \\ \phi_j^{*T}\cdot\mathbf{F}^*\cdot V_f\cdot\frac{b_s^2 L}{\bar{V}}\cdot\bar{m} \end{pmatrix}$$

For the novel FSI procedure [16] adopted in this study, all mode shapes must be given at the CFD mesh on the blade surface. If mode shapes are not available from the manufacturer, CFD mesh is usually used as boundary points for FE analysis. In this study, the mode shapes provided by the engine manufacturer are used by applying an interpolation in order to match the mode shape data to the present CFD mesh on the blade surface. Once the $q_j(t)$ is determined, the physical displacements are obtained by the mode summation procedure, which is given in Eq. (6) and can be expressed in terms of vibration mode as

$$x_i = \sum_j \tilde{\Phi}_j(x_i) q_j(t) \tag{11}$$

where the subscript i denotes the ith grid point of the blade surface mesh. Note that additional efforts on aerodynamic force transfer between the fluid flow and the structural solver, which is necessary for a loosely coupled non-monotonic approach in which two distinct (or separate) flow and structural solvers are used [13], are not needed with current fully coupled FSI approach. The mode shapes given at each grid point are redefined on the cell center point using simple interpolation within the solver. In this way, the aerodynamic force estimated on each cell center of the blade surface mesh are directly used to solve the modal equations given by Eq. (9).

4.2 Implicit Structural Solver

To solve the structural equations with the CFD solver [20, 30] in a fully coupled manner, the decoupled structural equations are integrated using the same method as the flow governing equations within each physical time step:

$$\begin{aligned}\left(\tfrac{1}{\Delta\tau}I + \tfrac{1.5}{\Delta t}M + K\right)\delta S^{n+1,m+1} \\ = q^{n+1,m+1} - M\tfrac{3S^{n+1,m} - 4S^n + S^{n-1}}{2\Delta t} - KS^{n+1,m}\end{aligned} \tag{12}$$

The fluid/structural interaction is implemented in a fully coupled manner [16]. Within each physical time step, the flow equations and structural equations are solved iteratively via successive pseudo time step until the prescribed convergence criteria are satisfied for both flow and structural solver. After the convergence criteria are reached, the fluid-structural interaction goes to next physical time step.

5 Computational Mesh

The 1/7th sector baseline mesh for 1-1/2 stage of the GE-C1 compressor is presented in Fig. 3. The rotor tip clearance is modeled with 11 grid points using an O-mesh block. The tip gap is shown to have a significant effect on overall performance of axial compressors [31]. The fully gridded tip mesh generation technique adopted in this study is shown to better predict the tip clearance flow than the pinched tip or simplified tip model [32]. In the model of the fully gridded tip, about 4 to 10 points in the tip clearance are generally considered as adequate to predict the primary effects of the leakage flow in axial compressor [31–34]. However, it is not possible to determine the precise impact of the tip clearance modeling on the flow solutions due to the lack of detailed flow measurements in the tip clearance of the NSV compressor.

The mesh of IGV/rotor/stator is partitioned to total 174 blocks for parallel computation. The mesh around blade was constructed by using the O-mesh. For the IGV and stator 121(around blade)×77(blade-to-blade)×46(blade span) is the mesh size, and for rotor 201(around blade)×77(blade-to-blade)×46(blade span). A H-mesh layer is used for the matched one-to-one grid point connection at the sliding BC interface of IGV/rotor/stator that enables variable exchange in a fully conservative manner. Each H-mesh layer has mesh size of 201(tangential)×6(axial)×46(blade span). The total mesh size for this 1/7 sector of 1-1/2 compressor is 6,142,467.

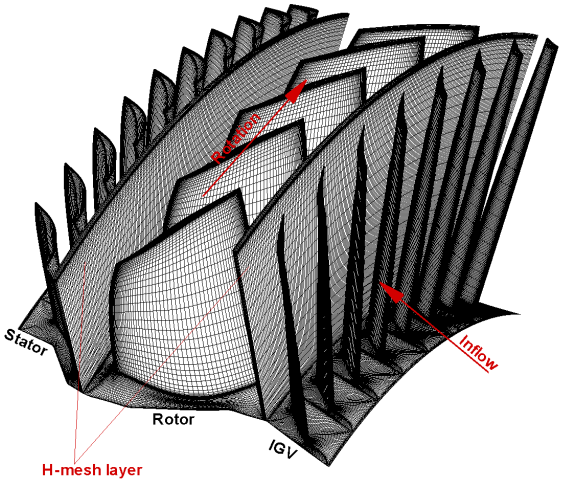

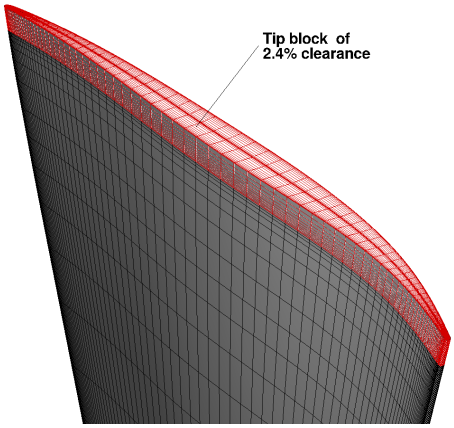

FIGURE 3: 1/7th Annulus baseline mesh for NSV simulation

6 Numerical Probes

The numerical probes to acquire static pressure responses on the blade surface and at the tip clearance are shown in Fig. 4. Total 60 points on each blade surface, 5 points in the middle of the tip clearance and 5 points at the casing surface are mounted. The first numeral of the probe number means location around blade surface and the second numeral indicates location of blade span. For example, the probe 64 means the 6th probe from the trailing edge and the 4th probe from the hub, which is on the suction surface of 93% blade span near leading edge.

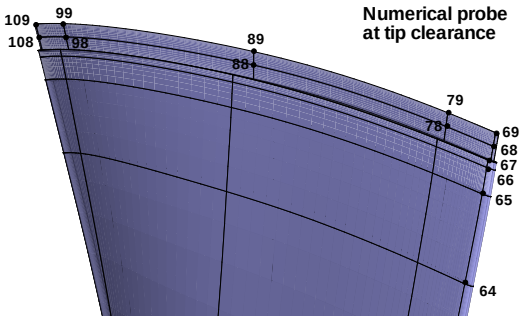

FIGURE 4: Numerical probes on the rotor blade

7 Blade Deforming Mesh

A CPU efficient deforming mesh technique is one of the requisites for FSI to accurately describe the vibration of the structure. The conventional method regenerates mesh inside domain with the fixed outer boundaries. However this may cause significant numerical instability due to the high mesh skewness when the vibrating structure is close to the boundaries like rotor tip clearance. In this study an advanced deforming mesh algorithm proposed by the present authors [17] is employed to improve mesh quality over rotor tip clearance. The basic idea is to reposition the casing grid points so as to keep high normality between the rotor tip and the casing. Once a blade-to-blade section is done, then 3D mesh is obtained by stacking each blade section from the hub to the tip. It has been shown by the present authors [27] that the test of this algorithm for a blade-to-blade section works robustly for the blade vibration.

8 Mode Shape of the 1st Stage Rotor Blade

Since the first a few modes are believed to be enough to describe turbomachinery blade vibration characteristics [17, 35], the first five mode shapes used in this study are normalized by the generalized mass($\sqrt{\phi^T m \phi}$) and provided by the manufacturer. The natural frequencies are 1041.42 Hz, 2658.02 Hz, 2988.68 Hz, 5180.21 Hz and 5890.47 Hz. The deflections of the first, second and third mode are displayed in Fig. 5. The blades are modeled as fixed at the rigid body rotor. Note that the NSV of the compressor under study is captured in the experiment close to the first torsional mode, which is mode 2 in Fig. 5.

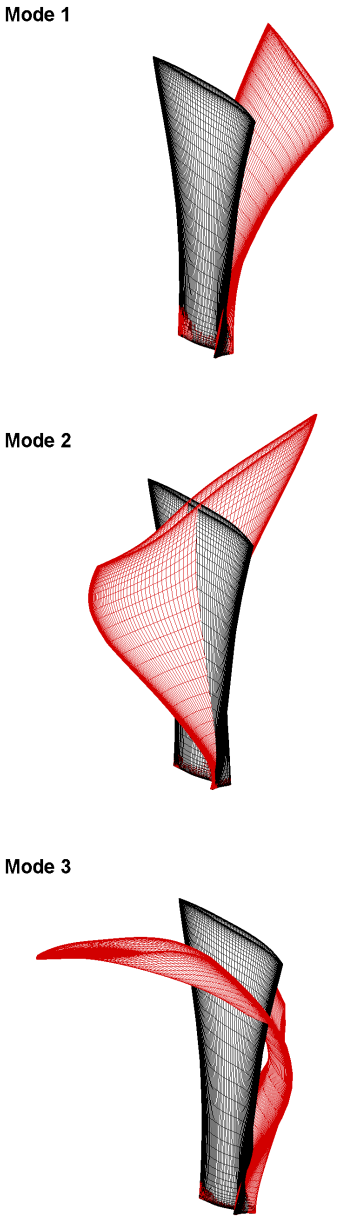

FIGURE 5: Rotor blade modal deflections; the 1st mode(top), the 2nd mode(middle), the 3rd mode(bottom)

9 Results and Discussion

The rig testing of the full axial compressor with 1.1% tip clearance [2, 10] is shown to have the NSV frequency range of 2600 Hz to 2661 Hz, which is located between 12EOL to 13EOL and is near the first torsional mode (1T) as shown in the Campbell diagram in Fig. 6. The compressor operating point used for the present NSV simulations is 2600 Hz at 12880 RPM. Note that EOL(engine order line) in Campbell diagram is obtained by integer multiples of rotor shaft frequency with respect to RPM. The Campbell diagram can be used to evaluate whether a blade frequency including natural frequency is synchronous or not with engine shaft. The present FSI simulation with 2.4% tip clearance shows the dominant frequency of 2365 Hz, which is a NSV between 11EOL and 12EOL. Note that a large tip clearance size of 2.4% tip chord is recommended by the engine manufacturer. The residual is reduced by three orders of magnitude within

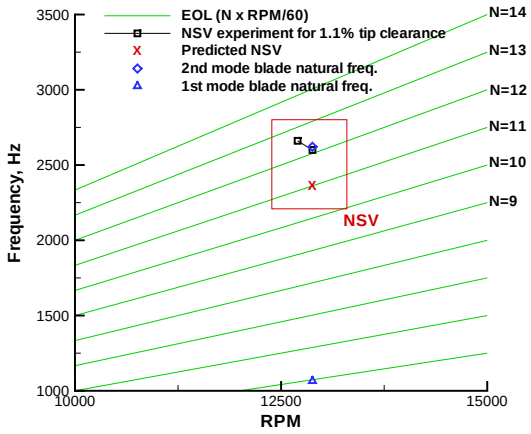

FIGURE 6: Campbell diagram of the compressor

each physical time step, which is usually achieved within 30 to 40 pseudo time step iterations. A non-dimensional time step of 0.005 is used.

9.1 Mesh Refinement Study

The mesh refinement study is conducted before the fully coupled FSI simulation [10]. For a finer mesh, the rotor tip clearance is modeled with 21 grid points using an O-mesh block. For the IGV and stator, 121(around blade)×101(blade-to-blade)×71(blade span) is the mesh size, and for the rotor, 201(around blade)×101(blade-to-blade)×71(blade span). The size of the H-mesh layer used for the matched one-to-one grid point connection at the sliding BC interface of IGV/rotor/stator is 201(tangential)×6(aixal)×71(blade span). The total mesh size for this 1/7 sector of 1-1/2 compressor is 12,127,638. As shown in Fig. 8, the total pressure ratio of Rotor-to-IGV and mass flow predicted by the baseline mesh is well converged to the fine mesh with about 0.5% difference. The IGV pass-

ing frequency predicted by the baseline mesh at about 50% span of rotor leading edge shows an excellent agreement with the fine mesh as presented in Fig. 7.

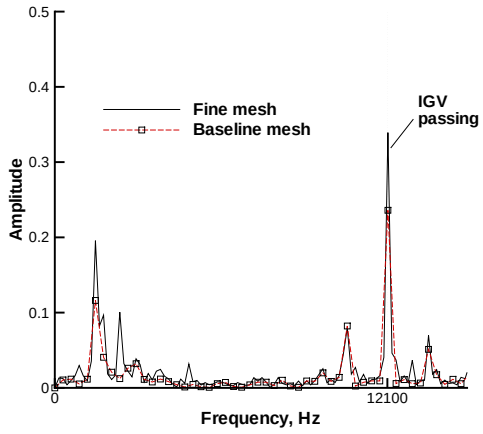

FIGURE 7: Predicted IGV passing frequencies at about 50% span from the mesh refinement study

9.2 The Speedline and NSV Location

Since NSV of axial compressors is typically observed in stable operation [1–4], unsteady flow simulations are first conducted with rigid blades and no vibration using a finer mesh at different back pressure conditions to find the dominant region of NSV in the speedline.

Fig. 8 shows the predicted speedline of the 1-1/2 stage axial compressor. Note that the time averaged speedline data for the fine mesh and the baseline mesh are obtained with rigid blades for mesh refinement study by averaging final 2 rotor revolutions.

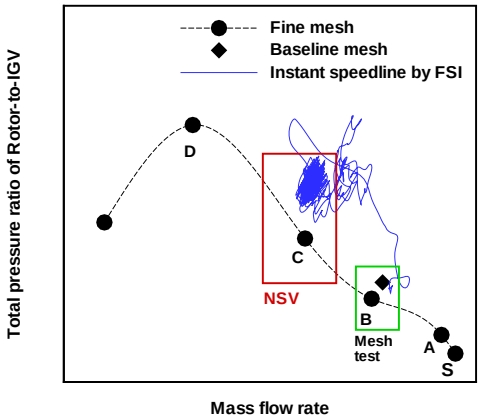

FIGURE 8: IGV-to-rotor speedline from the fully coupled FSI

The point A, B, C and D represent rotor-to-IGV total pressure characteristics. The back pressure is gradually increased from the point S to find the near stall point D. After the point D the compressor stalls. The point S is about maximum mass flow condition. No NSV events are found at point S. The mass flow rate obtained at the point C is about 6% higher than the near stall point D.

The unsteady FSI simulation is started from the solutions obtained at the point B. The back pressure used at the point B is slightly increased to obtain about the same mass flow near the point C. The NSV of 2365 Hz is obtained by the NSV simulation based on the fine mesh with rigid blades. As illustrated in Fig. 8, the instant speedline predicted by the FSI simulation with the baseline mesh converges well to the point C. The same NSV frequency of 2365 Hz is observed by the fully coupled FSI.

Fig. 9 shows time history of the rotor outlet mass flow rate during the NSV predicted by the fully coupled FSI. In this study the unsteady solutions between 0.5 and 2 rotor revolutions are used for the NSV frequency analysis since the predicted mass flow shows periodic oscillations after 0.5 revolution. It is clear that the compressor under the NSV operates without the mass flow breakdown as presented by the experimental studies [1–4].

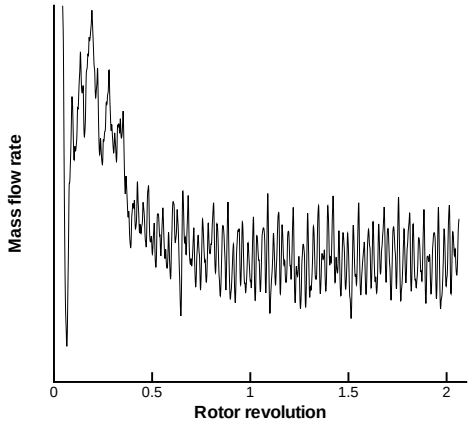

FIGURE 9: Instantaneous mass flow during NSV from the fully coupled FSI

9.3 NSV Simulation Using the Fully Coupled FSI

As aforementioned, the flow instabilities around the rotor tip are the main causes of NSV [2, 3, 10].

The axial velocity contour at the blade tip span is shown in Fig. 10. There is a large area of the negative axial velocity near the rotor leading edge due to the tornado vortices during the NSV [10]. A strong interaction of the tornado-like vortices with incoming flow of the IGV downstream is observed near the rotor leading edge [10].

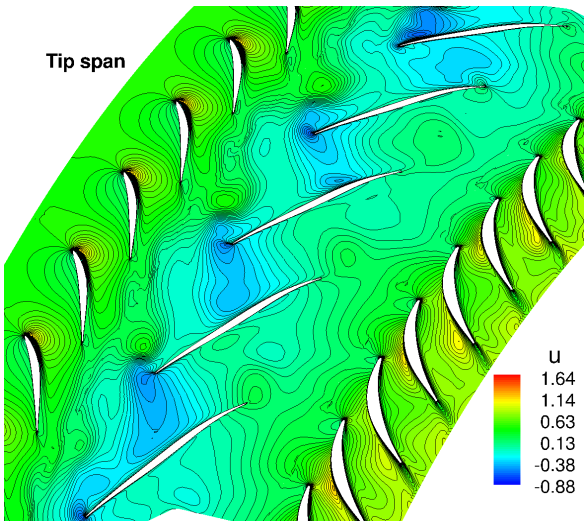

FIGURE 10: Axial velocity contour at tip span from the fully coupled FSI

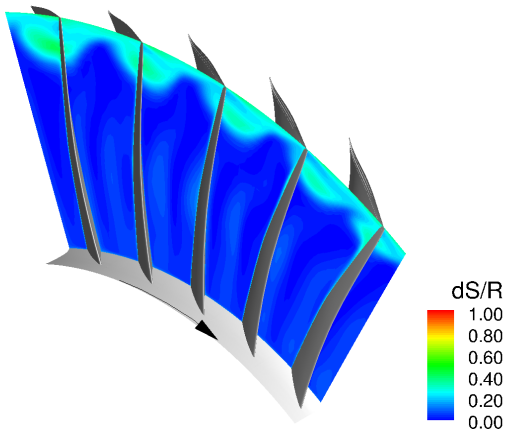

FIGURE 11: Entropy contour of the axial plane near the rotor leading edge from the fully coupled FSI

Fig. 11 shows entropy contour of the axial plane near rotor leading edge. Entropy stands for the degree of energy loss, hence high entropy reflects high disturbance due to the flow separation. Entropy is significantly increased for the flow field about 20% span from the casing, where the tornado-like vortex interacts with the main flow as presented in Fig. 12. The 3D tornado like tip vortex structure is very different from the regular streamwise tip clearance vortex. It swirls strongly with vortex axis normal to the blade suction surface around the rotor leading edge, oscillates within each blade passage and creates the flow instability that causes the NSV. The static pressure at 78% span near the rotor leading edge highly fluctuates during the NSV due to the tornado vortex oscillation in the streamwise direction [10]. The NSV of 2365 Hz with maximum amplitude is observed at roughly 78% span near leading edge of the rotor (probe 63 in Fig. 4). The boundary of the vortical flow dominant flow is around 78% span, where the strong interaction exits with entropy jump as shown in Fig. 11.

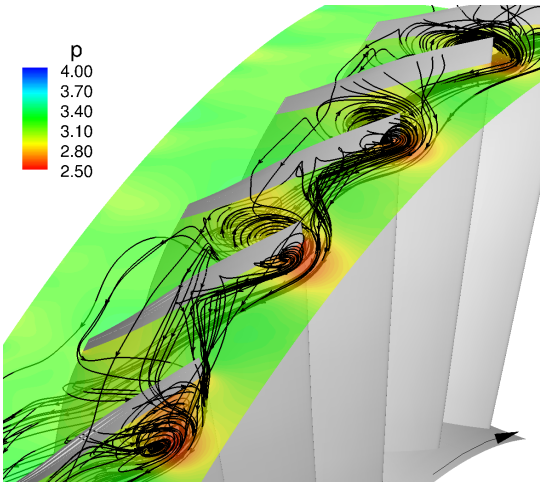

FIGURE 12: Tornado like tip vortices with static pressure contour around tip vortex center from the fully coupled FSI

Instantaneous blade surface pressure acquired at 78% span and tip clearance are plotted in Fig. 13. The maximum amplitude of the pressure is observed at 78% span near the rotor leading edge. The tornado tip vortex as illustrated in Fig. 12 is shown to cause strong interaction between incoming flow and tip leakage, which explains why the peak NSV is observed at the 78% span near the rotor leading edge. It should be emphasized by the NSV experiment of Baumgartner et al. [1] that the hot-film measurements of the 1st stage rotor blades show the radial dependency of the rotating instability as the main driver of the NSV observed for the 10 stage high pressure axial compressor. The NSV with high blade vibration amplitude is observed between 65% to 91% of the blade span, while the measurements close to the casing wall are very noisy without high fluctuations. The compressor investigated in this study is an aircraft engine high speed full compressor similar to the compressor used for the NSV experiment of Baumgartner et al. [1] and also exhibits the NSV in the 1st stage rotor blades.

It is clear that fluctuation level of the pressure is significantly amplified at78% span near the rotor leading edge. It is shown by the NSV experiments [1, 3, 4] that the blade sensor signals under the NSV have a strong periodic content due to the rotating instability near the rotor tip region. The present numerical simulation using a fully coupled FSI clearly demonstrates a strong periodic oscillation of the blade surface pressure during the NSV.

The modal force($\frac{\tilde{\phi}_j^{*T}}{m_j^*} \cdot \mathbf{F}^* \cdot {V_f}^2 \cdot \frac{b_s^2 L_\infty}{\bar{V}} \cdot \bar{m}$) acting on a blade is shown in Fig. 14. The fluctuation of the second modal force is much larger than that of the first mode and the third mode. The oscillating pattern is a phase-locked and periodic, which is very similar with the pressure signal acquired at

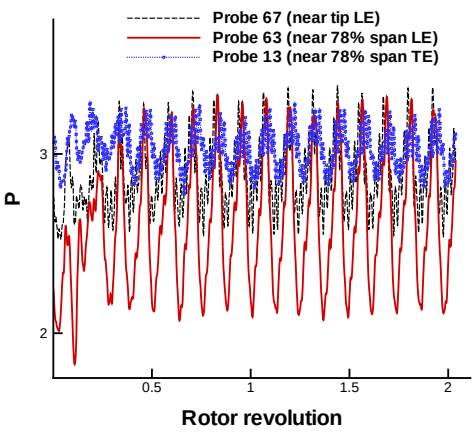

FIGURE 13: Instantaneous pressure acquired at the blade 3 during NSV from the fully coupled FSI

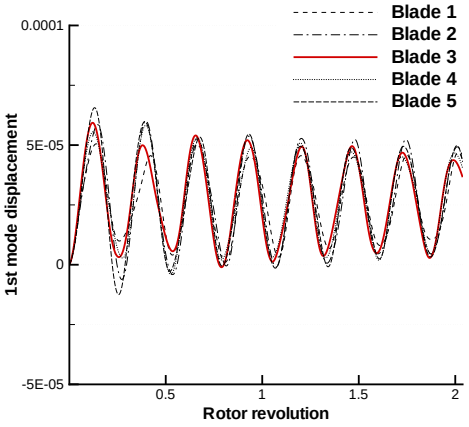

FIGURE 15: 1st mode displacements during NSV from the fully coupled FSI

78% span near leading edge. The rotor blades are excited due to the highly oscillating aerodynamic force induced by the tornado vortex instability during the NSV. In this way, the first stage rotor blades vibrate with a high amplitude near the second mode.

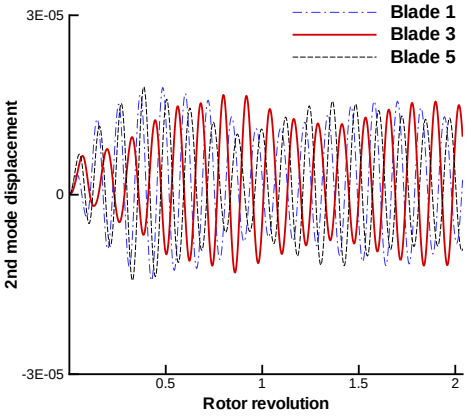

FIGURE 16: 2nd mode displacements during NSV from the fully coupled FSI

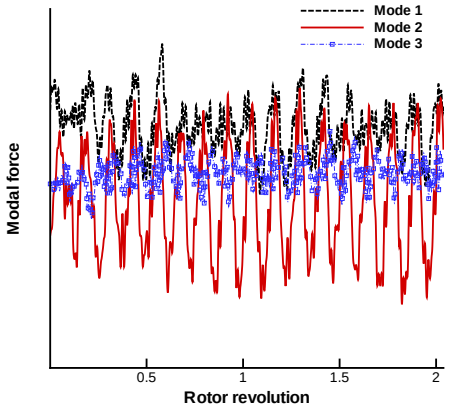

FIGURE 14: The blade modal force($\frac{\tilde{\phi}_j^{*T}}{m_j^*} \cdot \mathbf{F}^* \cdot {V_f}^2 \cdot \frac{b_s^2 L_\infty}{\bar{V}} \cdot \bar{m}$) during NSV from the fully coupled FSI

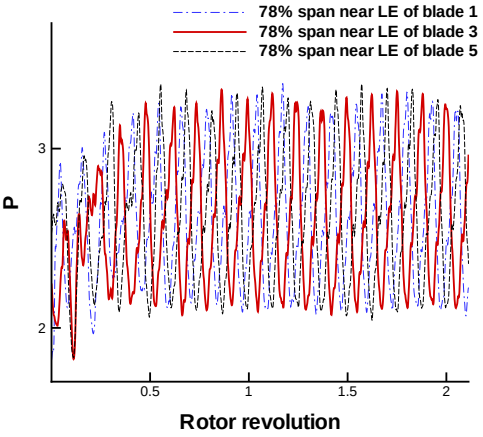

FIGURE 17: Instantaneous pressure acquired at 78% span near leading edge during NSV from the fully coupled FSI

Fig. 15 and Fig. 16 show the first, the second modal displacements respectively during the NSV. The responses of the first mode are being damped out. The displacements of the second mode (torsion) do not diverge nor decay in time, which is the typical nonlinear vibration pattern of limited cycle oscillation (LCO). If the NSV of the 1st stage rotor blades captured in this study is a flutter like blade instability, the blade responses then must be a kind of divergent-amplitude response with increasing time. However, the blade vibration predicted by the present FSI simulation clearly is a LCO that may cause high cycle fatigue(HCF) of the blade structure.

Unfortunately no experimental measurement with regard to the unsteady pressure responses of the compressor blades is available. However, such an experiment of Baumgartner et al. [1] could be used as the qualitative comparison reference for the present study since the compressors at high-speed regime with similar design specifications. The NSV experiments [1,3,4] show that the high amplitude blade signals under NSV oscillates in a periodic manner.

As shown in Fig. 16 and Fig. 17, a strong coupling between the pressure at 78% span of the blade and the second mode of the blade frequency exists during the NSV. The same NSV frequency of 2365 Hz is obtained at 78% span near the rotor leading edge using the blade displacement and the fluid pressure as plotted in Fig. 18. Therefore, it is obvious that the blade pressure signal causes the second mode vibration during the NSV. In conclusion, the present FSI for the high-speed compressor demonstrates the reason why the NSV occurs near the second mode (or the first torsional mode) in the experiment [2].

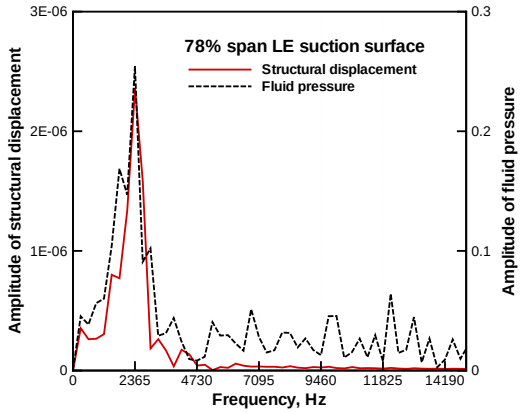

FIGURE 18: Comparison of frequencies using the structural displacement and the fluid pressure at 78% near LE suction surface during the NSV from the fully coupled FSI

Fig. 19 represents the modal displacements of the blade 3. The first two modal displacements are dominant, which indicates that use of first five mode shapes are reasonable to describe the blade vibration during the NSV because the blade displacements for the rest of higher modes are very small.

It is meaningful to see the vibration at the blade tip leading edge where in general the largest displacement is observed. Fig. 20 shows the net tangential physical displacement at the rotor tip leading edge, where y_o, z_o denotes y-, z-coordinates of initial blade position. It is shown that the blade vibration is not a pure harmonic mode and at least two modes(the first bending and the first torsion) are combined within a cycle.

Frequency analysis using the blade displacements at the tip leading edge is presented in Fig. 21. ω_2 represents the

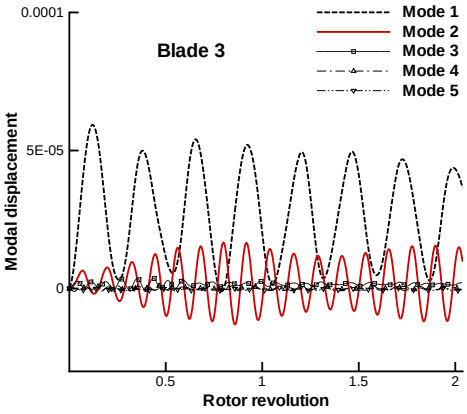

FIGURE 19: Five modal displacements of the blade 3 during NSV from the fully coupled FSI

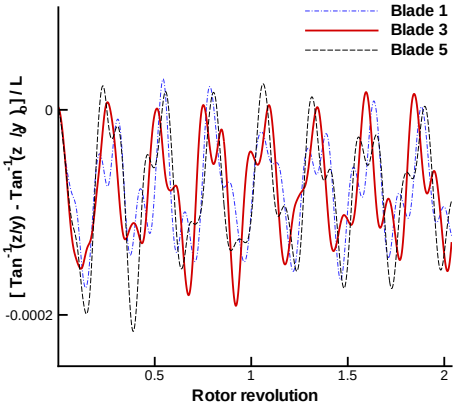

FIGURE 20: Normalized net tangential displacements at the rotor tip LE during NSV from the fully coupled FSI

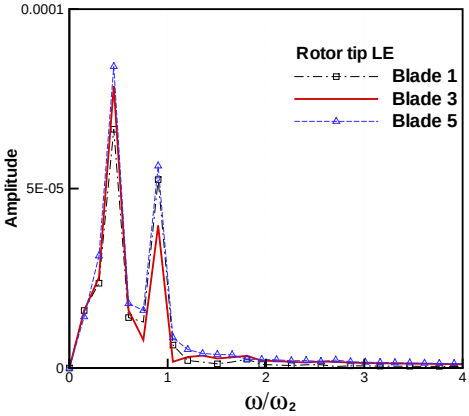

FIGURE 21: Predicted frequencies using the tip displacements from the fully coupled FSI

blade second mode natural frequency of around 2621 Hz. Note that the mode summation procedure given by Eq. (11) is used to obtain the physical displacements in the modal approach. The predicted frequency ratio($\frac{\omega}{\omega_2}$) indicates no resonance with blade natural frequencies during the NSV.

Two dominant frequencies are captured at the rotor tip leading edge during the NSV. The frequency ratio of about 0.9 is the NSV frequency of 2365 Hz, which is about 9% lower than the frequency of the rig testing of the axial compressor with 1.1% tip clearance [2]. The frequency ratio of about 0.45 is around the first mode of the blade natural frequency, which is not a primary NSV frequency by the experiment [2]. However, use of such a large tip clearance gives rise to stall in the vicinity of rotor tip due to the largely separated flow, as a consequence the blades can vibrate at a low frequency.

Fig. 22 shows the 3D tornado like tip vortex structure with vorticity. In the region of 78% span leading edge, the vorticity is high because there exists a strong interaction of incoming flow, tip tornado vortices and tip leakage flow, which appears to be the instability causing the NSV. Fig. 22 also indicates that the tip tornado vortex of a blade is not formed primarily by its own tip leakage jet, but by the tip leakage jet from the adjacent upstream blade and the jet interaction with the incoming flow.

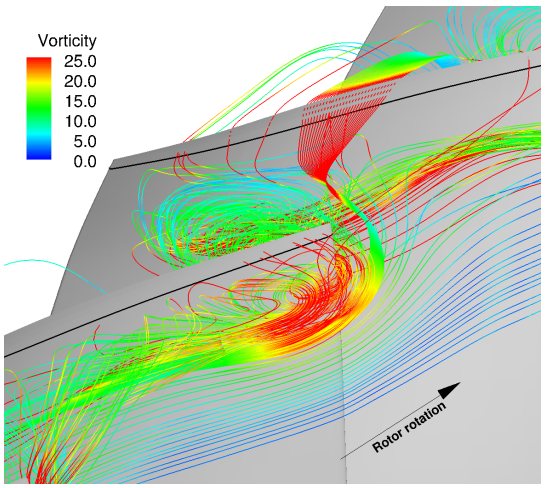

FIGURE 22: Tip tornado vortices during NSV from the fully coupled FSI

10 Conclusions

The NSV is simulated using a fully coupled fluid-structural interaction for a GE axial compressor. A fully conservative sliding BC is used with a time shift method in the lower/upper circumferential periodic boundaries for a 1-1/2 stage unsteady simulation.

A tip clearance of 2.4% tip chord is used in the simulation and the predicted NSV frequency of 2365 Hz is about 9% lower than the frequency of the rig testing with 1.1% tip clearance. The predicted NSV frequency is the same as the one predicted using rigid blades with no vibration.

The blade NSV is strongly coupled with unsteady aerodynamic pressure oscillation at 78% span near the rotor leading edge induced by the tip tornado vortex. The oscillation of these tornado vortices due to the strong interaction of incoming flow, tip vortex and tip leakage flow is the main cause of the NSV observed in this study.

Acknowledgement

We thank GE for approving publishing the results. We greatly appreciate the help of Gerardo "LC" Colmenero and Steve Manwaring at GE Aviation for providing the compressor geometry and testing data. The grants support from AFRL and the industrial partners of GUIde Consortium, 10-AFRL-1024 and 09-GUIDE-1010, are acknowledged. The numerical simulations are conducted at the Center for Computational Sciences at the University of Miami and Air Force Research Lab DoD Supercomputing Resource Centers.

REFERENCES

[1] M. Baumgartner, F. Kameier, and J. Hourmouziadis, "Non-Engine Order Blade Vibration in a High Pressure Compressor." ISABE, Twelfth International Symposium on Airbreathing Engines, Melbourne, Australia, 10-15, 1995.

[2] R. Kielb, J. Thomas, P. barter, and K. Hall, "Blade Excitation by Aerodynamic Instabilites - A Compressor Blade Study." ASME Paper No. GT-2003-38634, 2003.

[3] J. Marz, C. Hah, and W. Neise, "An Experimental and Numerical investigation Into the Mechanisms of Rotating instability," *Journal of Turbomachinery*, vol. 124, pp. 367–375, 2002.

[4] R. Mailach, I. Lehmann, and K. Vogeler, "Rotating Instabilites in an Axial Compressor Originating From the Fluctuating Blade Tip Vortex." ASME Paper No. GT-2003-38634, 2003.

[5] J. Thomassin, H. Vo, and N. Mureithi, "Blade Tip Clearance Flow and Compressor Nonsynchronous Vibrations: The Jet Core Feedback Theory as the Coupling Mechanism," *Journal of Turbomachinery*, vol. 131, pp. 11013–1–11013–9, 2009.

[6] J. Thomassin, H. Vo, and N. Mureithi, "The Tip Clearance Flow Resonance Behind Axial Compressor Nonsynchronous Vibration," *Journal of Turbomachinery*, vol. 133, pp. 041030–1–041030–10, 2011, doi:10.1115/1.4001368.

[7] A. Sanders, "Nonsynchronous Vibration(NSV) due to a Flow-Induced Aerodynamic Instability in a Composite Fan Stator," *Journal of Turbomachinery*, vol. 127, pp. 412–421, 2005.

[8] Vo, H.D., "Role of Tip Clearance Flow in Rotating Instabilities and Nonsynchronous Vibrations," *Journal of Propulsion and Power*, vol. 26, pp. 556–561, doi: 10.2514/1.26709, 2010.

[9] A. Carter, and D. Kilpatrick, "Self-excited vibration of axial-flow compressor blades," *Proceedings of the Institution of Mechanical Engineers 1847-1996*, vol. 171, pp. 245–281, 1957, DOI:10.1243/PIME_PROC_1957_171_030_02.

[10] H.S. Im, and G.C. Zha, "Effects of Rotor Tip Clearance on Non-synchronous Blade Vibration for an Axial Compressor." ASME GT2012-68148, 2012.

[11] R. Kamakoti, and W. Shyy, "Fluid.structure interaction for aeroelastic applications," *Progress in Aerospace Sciences*, vol. 40, pp. 535–558, 2004.

[12] V. Gnesin, and R. Rzadkowski, "A Coupled Fluid-Structure Analysis for 3-D Inviscid Flutter of IV Standard Configuration," *Journal of Sound and Vibration*, vol. 251, pp. 315–327, 2002.

[13] H. Doi, and J.J. Alonso, "Fluid/Structure Coupled Aeroelastic Computations for Transonic Flows in Turbomachinery." GT2002-30313,Proceedings of ASME Turbo Expo 2002, 2002.

[14] V. Carstens, R. Kemme, and S. Schmitt, "Coupled Simulation of Flow-srtuctrue Interaction in Turbomachinery," *Aerospace Science and Technology*, vol. 7, pp. 298–306, June 2003.

[15] A.I. Sayma, M.V. Vahdati, and M. Imregun, "Turbine Forced Response Prediction Using an Integrated Nonlinear Analysis," *Proceedings of the Institution of Mechanical Engineers, Part K: Journal of Multi-body Dynamics*, vol. 214, pp. 45–60, 2000.

[16] X.Y. Chen, G.-C. Zha, M.-T. Yang, "Numerical Simulation of 3-D Wing Flutter with Fully Coupled Fluid-Structural Interaction," *Journal of Computers & Fluids*, vol. 36, pp. 856–867, 2007.

[17] H.-S. Im, X.-Y. Chen, and G.-C. Zha, " Detached Eddy Simulation of Transonic Rotor Stall Flutter Using a Fully Coupled Fluid-Structure Interaction." ASME GT2011-45437, ASME Turbo Expo 2011, Vancouver, Canada, June 2011, 2011.

[18] H.S. Im, X.Y. Chen, and G.C. Zha, "Detached Eddy Simulation of Rotating Stall for a Full Annulus Transonic Rotor," *Journal of Propulsion and Power*, to appear.

[19] P.R. Spalart, W.H. Jou, M. Strelets, and S.R. Allmaras, "Comments on the Feasibility of LES for Wings, and on a Hybrid RANS/LES Approach." Advances in DNS/LES, 1st AFOSR Int. Conf. on DNS/LES, Greyden Press, Columbus, H., Aug. 4-8, 1997.

[20] G.C. Zha, Y.Q. Shen, and B.Y. Wang, "An improved low diffusion E-CUSP upwind scheme ," *Journal of Computer and Fluids*, vol. 48, pp. 214–220, 2011, doi:10.1016/j.compfluid.2011.03.012.

[21] Y.Q. Shen, G.C. Zha, and B.Y. Wang, "Improvement of Stability and Accuracy of Implicit WENO Scheme," *AIAA Journal*, vol. 47, pp. 331–334, DOI:10.2514/1.37697, 2009.

[22] Y.Q. Shen, B.Y. Wang, and G.C. Zha, "Implicit WENO Scheme and High Order Viscous Formulas for Compressible Flows ." AIAA Paper 2007-4431, 2007.

[23] B. Wang, Z. Hu, and G. Zha, "A General Sub-Domain Boundary Mapping Procedure For Structured Grid CFD Parallel Computation," *AIAA Journal of Aerospace Computing, Information, and Communication*, vol. 5, pp. 425–447, 2008.

[24] H.S. Im, X.Y. Chen, and G.C. Zha, "Simulation of 3D Multistage Axial Compressor Using a Fully Conservative Sliding Boundary Condition." ASME IMECE2011-62049, International Mechanical Engineering Congress & Exposition, Denver, November 2011, 2011.

[25] J.I. Erods, E. Alzner, and W. McNally, "Numerical solution of periodic transonic flow through a fan stage," *AIAA Journal*, vol. 15, pp. 1559–68, Nov. 2004.

[26] R. Srivastava, M.A. bakhle, T.G. Keith Jr, and G.L. Stefko, "Aeroelastic analysis of turbomachinery: Part I-phase lagged boundary condition methods," *International Journal of Numerical Methods for Heat & Fluid Flow*, vol. 14, pp. 366–381, Nov. 2004.

[27] H.-S. Im, and G.-C. Zha, " Flutter Prediction of a Transonic Rotor Using a Phase-lagged Boundary Condition." Proceedings of 50th AIAA Aerospace Sciences Meeting including the New Horizons Forum and Aerospace Exposition, Nashville, Tennessee, Jan 2012, 2012.

[28] B. Gruber, and V. Carstens, "The impact of Viscous Effects on the Aerodynamic Damping of Vibrating Transonic Compressor Blades - A Numerical Study," *Journal of Turbomachinery*, vol. 123, 2001.

[29] A. Srinivasan, "Flutter and Resonant Vibration Characteristics of Engine Blades." ASME 97-GT-533, October 1997.

[30] G.C. Zha, Y.Q. Shen, and B.Y. Wang, "Calculation of Transonic Flows Using WENO Method with a Low Diffusion E-CUSP Upwind Scheme." AIAA Paper 2008-0745, 46th AIAA Aerospace Sciences Meeting, Reno, NV, Jan. 2008.

[31] J. Denton, "Lessons from Rotor 37," *Journal of Thermal Science*, vol. 6, pp. 1–13, 1996.

[32] J. Dunham, "CFD Validation for Propulsion System Components." AGARD-AR-355, 1998.

[33] R. V. Chima, "Calculation of Tip Clearance Effects in a Transonic Compressor," *AMSE J. of Turbomach.*, vol. 120, pp. 131–140, 1998.

[34] J.P. Chen, M.D. Hathaway, and G.P. Herrick, "Prestall Behavior of a Transonic Axial Compressor Stage via Time-Accurvate Numerical Simulation," *AMSE J. of Turbomach.*, vol. 130, pp. 1–12, 2008.

[35] V. Gnesin, R. Rzadkowski, "A Coupled Fluid-Strcuture Analysis for 3D Flutter in Turbomachines." Proceedings of ASME Turbo Expo 2000, Munich, Germany, 2000.